Received: 26 April 2020 | Revised: 11 November 2020 | Accepted: 6 January 2021

DOI: 10.1002/nme.6632

RESEARCH ARTICLE

WILEY

Implementation of the coupled two-mode phase field crystal model with Cahn–Hilliard for phase-separation in battery electrode particles

Karthikeyan Chockalingam | **Willy Dörfler**

Institute for Applied and Numerical Mathematics, Karlsruhe Institute of Technology, Karlsruhe, Germany

Correspondence
Willy Dörfler, Institute for Applied and Numerical Mathematics, Karlsruhe Institute of Technology, Karlsruhe, Germany.
Email: willy.doerfler@kit.edu

Abstract

In this article, we present the behavior of two-mode phase field crystal (2MPFC) method under a concentration dependent deformation. A mixed finite element formulation is proposed for the 2MPFC method that solves a 10th-order parabolic equation. Lithium concentration diffusion in the electrode particle is captured by the Cahn–Hilliard (CH) equation and the host electrode material, $Li_xMn_2O_4$ (LMO), which has a face-centered cubic (fcc) lattice structure, is modeled using 2MPFC. The coupling between 2MPFC and CH models brings about the concentration dependent deformation in the polycrystalline LMO electrode particle. The atomistic dynamics is assumed to operate on a faster time-scale compared to the diffusion of lithium, thereby both the 2MPFC and CH models evolve on two different time-scales. The coupled 2MPFC–CH system models the diffusion induced grain boundary migration in LMO capturing the charging and discharging state of the battery.

KEYWORDS

Cahn–Hilliard, finite elements, phase field crystal, phase-separation

1 | INTRODUCTION

A lithium-ion battery is an electrical device consisting of two electrodes, namely anode and cathode, which are separated by an electrolyte.[1,2] One of the commonly used electrode particles in lithium-ion batteries is lithium manganese oxide spinel $Li_xMn_2O_4$ (LMO).[3] Considering the case when the battery is in discharge mode, lithium-atoms migrate from the interior of the anode-particle to the interface between the anode-particle and the electrolyte. At this point, they are oxidized into Li^+-ions and enter the electrolyte. In the electrolyte region, these ions migrate toward the cathode. As they reach the interface between the electrolyte and cathode-particle, they are reduced back to lithium atoms. This intercalation process creates two different phases within the electrode particle, a lithium-rich phase and lithium-depleted phase.[4]

Li-ions diffuse into preferential sites in the host electrode material. This intercalation process is highly complex and can structurally transform the electrode material,[5] resulting in defect formation,[6] lattice expansion,[7] grain boundary migration[8] and fracture.[9] One can potentially use molecular dynamics (MD)[10] to model the electrode and simulate the diffusion of Li-ions or use density function theory (DFT)[11] to study local preferential sites of Li-atoms. Although MD and DFT can capture certain effects in great detail, both cannot completely model the phase-separation process in a

---

electrode particle. While MD does not reach time-scales of hours, DFT cannot model more than few hundred atoms. The charging and discharging of a battery can take hours[12] and the average size of an electrode particle can vary from hundreds of nanometers to few micron meters.[13] Therefore, one has to rely on continuum techniques such as the phase field method[14,15] to overcome limitations posed by MD and DFT. As phase field methods seek to homogenize atomistic processes, they do not capture the change in structural transformation in the host electrode material due to lithiation.

Here we take a multi-scale approach[16,17] to study the phase transition in electrode particles by coupling the Cahn–Hilliard (CH) model[18] and the phase field crystal method.[19] The phase-field-crystal (PFC) method is proposed to study the material behavior of crystalline solids, which was previously only possible using atomistic models. The PFC model[19] has its origins in the Swift–Hohenberg (SH) model[20] for pattern formation but is reformulated to have conserved dynamics. It incorporates the effects of elastic interactions and dislocations due to perturbation of the field density.[21] Just like in DFT, the PFC method represents the material as a functional of its density. But unlike in DFT, the field density is only limited to a few number of reciprocal lattice vectors.[22] This approximation allows PFC to model certain crystalline structures for larger length and time scales.[23] The PFC method has been successfully applied to study problems such as crack propagation,[19] dislocation dynamics,[24] grain growth,[25] grain boundaries,[26] and solid to liquid transition.[27] The crystal field density ψ can be expressed as the sum of wave densities[28]

$$\psi = \psi_0 + \sum_{j=1}^{n} \left(A_j e^{\mathrm{i} q_j \cdot x} + A_j^* e^{-\mathrm{i} q_j \cdot x} \right), \tag{1}$$

where ψ_0 is the mean field density, A is the amplitude of the wave, and q denotes reciprocal lattice vectors. The free energy functional has the form

$$\mathscr{F} = \int_\Omega f(\psi, \Delta\psi)\, \mathrm{d}\boldsymbol{x}$$

with the one-mode free energy density[22]

$$f(\psi, \Delta\psi) = \frac{1}{2}\psi(\boldsymbol{x}) \left(a + \lambda\left(\Delta + q_0^2\right)^2 \right) \psi(\boldsymbol{x}) + \frac{g}{4}\psi(\boldsymbol{x})^4,$$

where λ, q_0, a, and g are phenomenological parameters. In this one-mode case, the sum of (1) is limited to wave vectors of magnitude $|q_j| = q_0$. This mode is suitable to model crystal lattice structures of the hexagonal and BCC type in two and three dimensions, respectively. The mode-two free energy density[22] can be expressed as

$$f(\psi, \Delta\psi) = \frac{1}{2}\psi(\boldsymbol{x}) \left(a + \lambda\left(\Delta + q_0^2\right)^2 \left(\left(\Delta + q_1^2\right)^2 + r \right) \right) \psi(\boldsymbol{x}) + g\frac{1}{4}\psi(\boldsymbol{x})^4,$$

where q_1 and r are phenomenological parameters. In this case, lattice vectors allow two different magnitudes, $|q_j| = q_0$ and $|q'_j| = q_1$. This mode is suitable to model crystal lattice structures of square and FCC type in two and three dimensions, respectively.

In this work, we limit our focus to capturing lattice expansion and grain boundary migration during phase separation. Since the phase field crystal method[23] works on atomistic length scale and diffusive time scales, it is used to model the host electrode material, while the CH equation models the diffusion of lithium-ions. This was first proposed by Balakrishna et al.,[29] where a one-mode phase field crystal method was used to model $FePO_4/Li_xFePO_4$ (LFPO) and CH to capture lithium diffusion. A transition matrix[25] was introduced to transform from hexagonal basis to rectangular basis to model $FePO_4/Li_xFePO_4$. This approach introduced an artifact resulting in atoms having an ellipsoidal shape. In this article, we directly work with the two-mode phase field crystal (2MPFC) method[22,30] suited to study cubic structures such as $Mn_2O_4/Li_xMn_2O_4$ (LMO).

Our choice of numerical scheme for this problem is based on finite-elements.[31,32] Although dependence of phase-separation on particle shape[33] is not part of the current work, it is known to have an significant impact and finite elements are especially suited to model arbitrarily shaped electrode particles. Such schemes have been already developed to study one-mode phase field crystal[34,35] with body-centered cubic (BCC) crystal structure. Work presenting simulations on 2MPFC[36-38] all use spectral methods to solve the system. In this article, we propose a mixed finite element formulation to solve the 2MPFC system, which is a 10th order parabolic equation, to model face-centered cubic (FCC) crystals.

The atomistic dynamics is assumed to operate on a faster time-scale compared to the diffusion of lithium, thereby both the 2MPFC and CH models evolve on two different time-scales. A composition-dependent coordinate transformation is introduced to include the effects of lattice expansion due to lithiation. The coupled 2MPFC–CH system was implemented within the MOOSE framework, an object-oriented finite element based solver for non-linear partial differential equations.[39]

In Section 2, a formulation to include lattice expansion in the free energy of the 2MPFC as a function of concentration is introduced. In Section 3, the framework used to solve the CH equation is presented. In Section 4, the finite element framework to couple 2MPFC and CH is presented. In Section 5, numerical results are presented to simulate a 2MPFC–CH system to model phase-separation in LMO in a multi-scale setting.

2 | TWO-MODE PHASE FIELD CRYSTAL MODEL

Let $\Omega \subset \mathbb{R}^2$ with points denoted by $\boldsymbol{x} = [x_1, x_2]$. In this article, Ω is always a rectangle. We define the differential operators $\boldsymbol{\nabla} = [\partial_1, \partial_2] \equiv [\partial_{x_1}, \partial_{x_2}]$, $\Delta = \boldsymbol{\nabla} \cdot \boldsymbol{\nabla} = \partial_1^2 + \partial_2^2$.

2MFPC energy. For sufficiently smooth $\psi : \Omega \to \mathbb{R}$, we denote its free energy of 2MPFC in dimensionless form corresponding to FCC symmetry as [22, Sect. 2.3]

$$\mathscr{F}(\psi) = \int_\Omega \frac{1}{2}\psi(\boldsymbol{x})G(\Delta)\psi(\boldsymbol{x}) + \frac{1}{4}\psi(\boldsymbol{x})^4 \,\mathrm{d}\boldsymbol{x} = \int_\Omega \frac{1}{2}\psi(\boldsymbol{x}) \left(-\varepsilon + (\Delta+1)^2 \left(\left(\Delta + Q^2\right)^2 + R\right)\right) \psi(\boldsymbol{x}) + \frac{1}{4}\psi(\boldsymbol{x})^4 \,\mathrm{d}\boldsymbol{x}, \tag{2}$$

can be obtained using the affine transformations

$$q_0\boldsymbol{x} \to \boldsymbol{x}, \quad \sqrt{\frac{g}{\lambda q_o^8}}\psi \to \psi, \quad \frac{g}{\lambda^2 q_0^{13}}\mathscr{F} \to \mathscr{F},$$

with

$$\varepsilon = -\frac{a}{\lambda q_0^8}, \quad R = \frac{r}{q_0^4}, \quad Q = \frac{q_1}{q_0},$$

where $\varepsilon > 0$, $Q \geq 0$, and $R \geq 0$ are dimensionless parameters controlling the phase, crystal symmetry, and relative amplitudes of density waves, respectively, and define the polynomial

$$G(s) = \left(-\varepsilon + (s+1)^2\left((s+Q^2)^2 + R\right)\right)$$

of fourth order.

In order to minimize the free energy $\mathscr{F}$, we need its variation $\mathscr{F}'(\psi)$ from which we obtain the gradient $\delta_\psi \mathscr{F}(\psi)$ that is defined by

$$\mathscr{F}'(\psi)[\phi] = \int_\Omega \delta_\psi \mathscr{F}(\psi)(\boldsymbol{x}) \; \phi(\boldsymbol{x}) \,\mathrm{d}\boldsymbol{x}$$

for all appropriate ϕ. Then a minimizer is approached by the parametric flow

$$\partial_\tau \psi(\tau, \cdot) = \Delta \delta_\psi \mathscr{F}(\psi(\tau, \cdot)). \tag{3}$$

Deformations. The aim of this presentation is to consider the behavior of the method under a concentration dependent deformation. We start with the energy (2) and assume that the actual domain $\tilde{\Omega}$ has been deformed out of the reference configuration Ω by some process. Thus starting from

$$\tilde{\mathscr{F}}(\tilde{\psi}) = \int_{\tilde{\Omega}} \frac{1}{2}\tilde{\psi}(\boldsymbol{y})G(\Delta)\tilde{\psi}(\boldsymbol{y}) + \frac{1}{4}\psi(\boldsymbol{y})^4 \,\mathrm{d}\boldsymbol{y}$$

we get by applying the deformation $\boldsymbol{y} : \Omega \to \tilde{\Omega}, \boldsymbol{x} \mapsto \boldsymbol{y}(\boldsymbol{x})$ the expression

$$\tilde{\mathcal{F}}(\tilde{\psi}) = \mathcal{F}(\psi) = \int_\Omega \left(\frac{1}{2}\psi(\boldsymbol{y})G(L)\psi(\boldsymbol{y}) + \frac{1}{4}\psi(\boldsymbol{y})^4\right)\det(\boldsymbol{\nabla}\boldsymbol{y}(\boldsymbol{x}))\,\mathrm{d}\boldsymbol{x}, \tag{4}$$

with $\psi(\boldsymbol{x}) = \tilde{\psi}(\boldsymbol{y}(\boldsymbol{x}))$ and L is a second order differential operator with respect to $\boldsymbol{x}$ due to the coordinate transformation.

We derive the form of the operator L in case of Δ. Let $\boldsymbol{y} \mapsto \boldsymbol{x}(\boldsymbol{y})$ be the inverse deformation and $A(\boldsymbol{x}) := \boldsymbol{\nabla}_{\boldsymbol{y}}\boldsymbol{x}(\boldsymbol{y}(\boldsymbol{x}))^t$ be its Jacobian. Then we have $\tilde{\boldsymbol{\nabla}}\tilde{\psi}(\boldsymbol{y}(\boldsymbol{x})) = A(\boldsymbol{x})\boldsymbol{\nabla}\psi(\boldsymbol{x})$ and by the transformation theorem

$$\int_{\tilde{\Omega}} \tilde{\Delta}\tilde{\psi}\ \tilde{\phi}\ \mathrm{d}\boldsymbol{y} = \int_\Omega \frac{1}{J}\boldsymbol{\nabla}\cdot\left(A^tJ\,A\boldsymbol{\nabla}\psi\right)\phi\ J\ \mathrm{d}\boldsymbol{x},$$

with $J(\boldsymbol{x}) := \det(\boldsymbol{\nabla}\boldsymbol{y}(\boldsymbol{x}))$. From this, we conclude

$$L\psi(\boldsymbol{x}) = \tilde{\Delta}\tilde{\psi}(\boldsymbol{y}(\boldsymbol{x})) = \frac{1}{J(\boldsymbol{x})}\boldsymbol{\nabla}\cdot\left(A(\boldsymbol{x})^tJ(\boldsymbol{x})\,A(\boldsymbol{x})\boldsymbol{\nabla}\psi(\boldsymbol{x})\right) = \frac{1}{J(\boldsymbol{x})}\boldsymbol{\nabla}\cdot\left(H(\boldsymbol{x})\boldsymbol{\nabla}\psi(\boldsymbol{x})\right),$$

where we let $H(\boldsymbol{x}) := A(\boldsymbol{x})^tJ(\boldsymbol{x})\,A(\boldsymbol{x})$. We further conclude for the biharmonic operator

$$\tilde{\Delta}^2\tilde{\psi} = \frac{1}{J}\boldsymbol{\nabla}\cdot\left(H\boldsymbol{\nabla}\left(\frac{1}{J}\boldsymbol{\nabla}\cdot(H\boldsymbol{\nabla}\psi)\right)\right),$$

and this continues to the higher order operators $\tilde{\Delta}^k$, $k=3,4$.

Concentration-induced deformation. We assume that Ω has been deformed by changing concentration, that is, $\tilde{\Omega} = \tilde{\Omega}(c)$. Following Reference 25, we insert the deformation gradient $\boldsymbol{\nabla}\boldsymbol{y}(\boldsymbol{x}) = 1/\alpha(c(\boldsymbol{x}))\,\boldsymbol{Id}$ into this model. We find $H(\boldsymbol{x}) = 1$ and $J(\boldsymbol{x}) = 1/\alpha(c(\boldsymbol{x}))^2$. Defining $\beta(c) = \alpha(c)^2$, we get the formulas

$$\begin{aligned} &\tilde{\boldsymbol{\nabla}}\tilde{\psi} = \sqrt{\beta}\ \boldsymbol{\nabla}\psi, && \tilde{\Delta}\tilde{\psi} = \beta\Delta\psi, && \tilde{\Delta}^2\tilde{\psi} = \beta\Delta(\beta\Delta\psi), \\ &\tilde{\Delta}^3\tilde{\psi} = \beta\Delta\left(\beta\Delta(\beta\Delta\psi)\right), && \tilde{\Delta}^4\tilde{\psi} = \beta\Delta\left(\beta\Delta\left(\beta\Delta(\beta\Delta\psi)\right)\right). \end{aligned}$$

We reduce the order of the resulting equation by introducing the additional states

$$\Delta\psi = \frac{1}{\beta}v, \quad \Delta v = \frac{1}{\beta}w, \quad \Delta w = \frac{1}{\beta}u, \quad \Delta u = \frac{1}{\beta}z,$$

that is, solving boundary value problems with boundary conditions $\boldsymbol{\nu}\cdot\boldsymbol{\nabla}\psi = 0$, and so on.

In the perturbed form, we now have

$$\mathcal{F}(\psi) = \int_\Omega \left\{\frac{1}{2}\psi G(\beta\Delta)\psi + \frac{1}{4}\psi^4\right\}\frac{1}{\beta}\ \mathrm{d}\boldsymbol{x}.$$

We write $G(s) = \sum_{k=0}^{4} a_k s^k$ and correspondingly we get

$$\mathcal{F}(\psi) = \sum_{k=0}^{4}\frac{1}{2}a_k\int_\Omega \psi(\beta\Delta)^k\psi\frac{1}{\beta}\ \mathrm{d}\boldsymbol{x} + \frac{1}{4}\int_\Omega \psi^4\frac{1}{\beta}\ \mathrm{d}\boldsymbol{x} = \frac{1}{2}\sum_{k=0}^{4}a_k\mathcal{J}_k(\psi) + \frac{1}{4}\int_\Omega \psi^4\frac{1}{\beta}\ \mathrm{d}\boldsymbol{x},$$

with the definition $\mathcal{J}_k(\psi)[\phi] := \int_\Omega \psi(\beta\Delta)^k\psi\frac{1}{\beta}\ \mathrm{d}\boldsymbol{x}$ for $k=0,\ \dots\ ,4$. In order to derive the formal derivative of $\mathcal{F}$ with respect to ψ, we can do this for $\mathcal{J}_k$, $k=0,\ \dots\ ,4$. This yields the representation providing us with a formula for $\delta_\psi\mathcal{F}(\psi)$

$$\begin{aligned} \mathcal{F}'(\psi)[\phi] &= \int_\Omega \left(\frac{1}{\beta}a_0\psi\phi - \boldsymbol{\nabla}\left(a_1\psi + a_2v + a_3w + a_4u\right)\cdot\boldsymbol{\nabla}\phi + \frac{1}{\beta}\psi^3\phi\right)\mathrm{d}\boldsymbol{x} \\ &= \int_\Omega \left(\frac{1}{\beta}a_0\psi + \Delta\left(a_1\psi + a_2v + a_3w + a_4u\right) + \frac{1}{\beta}\psi^3\right)\phi\ \mathrm{d}\boldsymbol{x}, \end{aligned}$$

where

$$a_0 = -\varepsilon + Q^4 + R, \qquad a_1 = 2(Q^2 + Q^4 + R), \qquad a_2 = 1 + 4Q^2 + Q^4 + R,$$
$$a_3 = 2(1 + Q^2), \qquad a_4 = 1.$$

In this derivation, we only consider the volume gradient of $\mathscr{F}$, that is, we neglect all boundary terms in the formal differentiation. For periodic boundary conditions, this would not be necessary.

We thus have to solve (3) starting from an initial state $\psi(0,\cdot) = \psi^0$. This amounts to an equation of 10th order in space, but we will reduce this into a system of second-order equations (10)–(14). The corresponding time-discretized system is given in (15)–(19).

Numerical validation. In the remainder of this section, we report on a validation of the proposed numerical scheme. We minimize (2) for an example with square symmetry in 2D, that is, the energy minimizing function ψ will be of the form

$$\psi_0(x_1, x_2) = \overline{\psi} + 2A\,(\cos(qx_1) + \cos(qx_2)) + 4B\;\cos(qx_1)\cos(qx_2). \tag{5}$$

Values for ε and $\overline{\psi}$ that correspond to a square phase can be chosen from the phase diagram in Figure 1. Inserting the (5) with $q = 1$, $\varepsilon = 0.15$, $R = 0$, $Q = \sqrt{2}$ and $\overline{\psi} = -0.23$ [22, Sect. 2.3] into (2) results in

$$\begin{aligned}\mathscr{F}(\psi_0) = {} & 2\left(-\epsilon + 3\overline{\psi}^{\,2}\right)A^2 + 2\left(-\epsilon + 3\overline{\psi}^{\,2} + R\right)B^2 + 24\overline{\psi}A^2B + 36A^2B^2 + 9A^4 \\ & + 9B^4 + \frac{1}{2}(4 + R - \epsilon)\,\overline{\psi}^{\,2} + \frac{1}{4}\overline{\psi}^{\,4}.\end{aligned} \tag{6}$$

A minimization of the above equation with respect to A and B gives $A \approx 0.10183$ and $B \approx 0.062177$. These values have been used to define an initial condition. An H^1- and L^2-error analysis for linear (P^1) and quadratic (P^2) elements compared to the steady solution ψ_0^h achieved using cubic C^1-elements over a periodic domain of size $6\pi \times 6\pi$ is performed. The results collected in Tables 1 and 2 show optimal convergence rates measured in the experimental order of convergence (eoc), given by $\mathrm{eoc}_k = 2\log(\mathrm{error}_k/\mathrm{error}_{k-1})/\log(N_{k-1}/N_k)$ (observe the relation $N \sim h^{-2}$ on uniform meshes in $\mathbb{R}^2$).

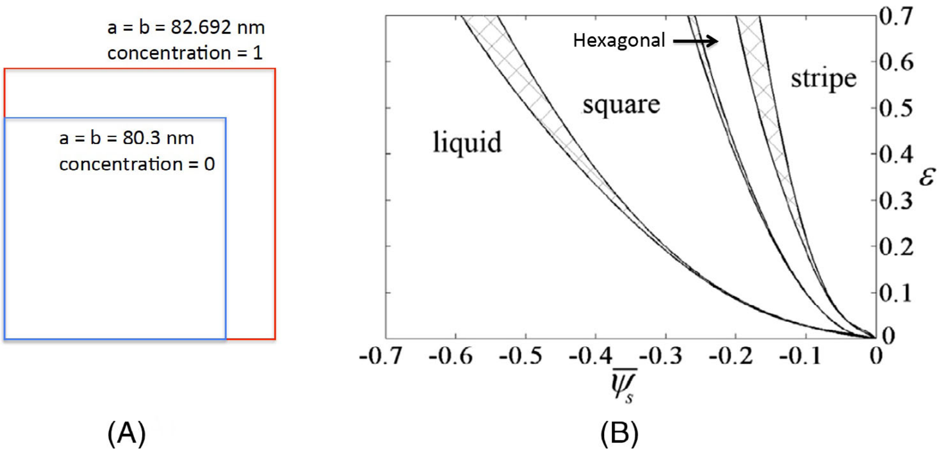

FIGURE 1 (A) Lattice expansion of LMO and (B) 2MPFC phase diagram taken from Reference 44 for $R = 0$ and $Q = \sqrt{2}$

TABLE 1 Error analysis for order one Lagrange elements (P^1)

N	H^1	eoc	L^2	eoc
1445	2.27_0		1.16_0	
5445	8.68_{-1}	1.45_0	8.25_{-2}	3.99_0
21,125	4.32_{-1}	1.03_0	1.68_{-2}	2.35_0
83,205	2.16_{-1}	1.01_0	4.12_{-3}	2.05_0

TABLE 2 Error analysis for order two Lagrange elements (P^2)

N	H^1	eoc	L^2	eoc
5445	2.63_{-1}		4.54_{-2}	
21,125	6.56_{-2}	2.05_0	5.88_{-3}	3.02_0
83,205	1.64_{-2}	2.02_0	7.43_{-4}	3.02_0
330,245	4.09_{-3}	2.01_0	9.30_{-5}	3.01_0

3 | CAHN–HILLIARD EQUATION

In this section, we study phase-separation of the lithium-rich and lithium-depleted phases in LMO material modeled by the CH equation. A logarithmic multi-well potential $W : [0,1] \to \mathbb{R}$, used in the bulk to study the two phases in dimensionless form,[3] is stated as

$$W(c) = \alpha_1 c + \frac{\alpha_2}{2} c^2 + c\ln(c) + (1-c)\ln(1-c),$$

where c presents the concentration of lithium and α_1, α_2 are constants that determine the height of the well.

The total free energy has contributions both from bulk energy and gradient energy. The latter arises due to the presence of a diffuse interface between the two phases. The gradient energy term is stated as $\kappa/2\ |\nabla c|^2$, where κ is the gradient energy coefficient, which is used to control the width of the interface. Thus the total energy $\mathscr{W}$ for a given concentration c is defined as

$$\mathscr{W}(c) = \int_\Omega W(c(\boldsymbol{x})) + \frac{1}{2}\kappa|\nabla c(\boldsymbol{x})|^2\ \mathrm{d}\boldsymbol{x}.$$

The variation of $\mathscr{W}$ with respect to c is expressed as

$$\mathscr{W}'(c)[\phi] = \int_\Omega \delta_c\mathscr{W}(c)(\boldsymbol{x})\phi(\boldsymbol{x})\ \mathrm{d}\boldsymbol{x} = \int_\Omega \big(W'(c(\boldsymbol{x})) - \kappa\Delta c(\boldsymbol{x})\big)\ \phi(\boldsymbol{x})\ \mathrm{d}\boldsymbol{x},$$

where ϕ is a continuously differentiable function.

From the following conserved dynamics, we seek $c : \mathbb{R}_{\geq 0} \times \Omega \to [0,1]$ satisfying the CH equation

$$\begin{aligned}\partial_t c(t,\cdot) &= \nabla \cdot (M(c(t,\cdot))\ \nabla\delta_c\mathscr{W}(c(t,\cdot))) \\ &= \nabla \cdot \big(M(c(t,\cdot))\ \nabla\big(W'(c(t,\cdot)) - \kappa\Delta c(t,\cdot)\big)\big),\end{aligned}$$

where $M(c)$ is the mobility. Here the mobility is taken as

$$M(c(t,\boldsymbol{x})) = D_0\ c(t,\boldsymbol{x})\ \ (1 - c(t,\boldsymbol{x})),$$

where D_0 is the diffusion coefficient of lithium. Since this amounts to an equation of fourth order in space, we will reduce this to a system of two second-order equations[40] for the concentration c and the chemical potential μ. The dynamics equation is thus split into

$$\begin{aligned}\partial_t c(t,\boldsymbol{x}) &= \nabla \cdot (M(c(t,\boldsymbol{x}))\ \nabla\mu(t,\boldsymbol{x})), \\ \mu(t,\boldsymbol{x}) &= W'(c(t,\boldsymbol{x})) - \kappa\Delta c(t,\boldsymbol{x}).\end{aligned}$$

4 | COUPLED 2MPFC–CH SYSTEM

The combined energy. In this section, we formulate a multi-scale scheme to study phase separation by coupling the 2MPFC and CH models together. The combined free energy functional is stated as

$$\mathscr{E}(c,\psi) = \int_\Omega \left(W(c(\boldsymbol{x})) + \frac{\kappa}{2}|\nabla c(\boldsymbol{x})|^2 + \gamma \left(\frac{1}{2}\psi(\boldsymbol{x}) G\left(\beta(c(\boldsymbol{x}))\Delta\right)\psi(\boldsymbol{x}) + \frac{1}{4}\psi(\boldsymbol{x})^4\right)\frac{1}{\beta(c(\boldsymbol{x}))}\right) \mathrm{d}\boldsymbol{x},$$

where γ relates the free-energy normalization of the CH and 2MPFC model. Here, in the case of LMO, we consider a model with stress generation under small strain assumption, therefore we treat the CH part as decoupled from the elastic part.[3] The deformation is thus applied in the second integral only.

We define the variations of $\mathscr{E}$ by

$$\partial_c \mathscr{E}(c,\psi)[\zeta] = \int_\Omega \delta_c \mathscr{E}(c,\psi)\ \zeta \ \mathrm{d}\boldsymbol{x} \quad \text{and} \quad \partial_\psi \mathscr{E}(c,\psi)[\phi] = \int_\Omega \delta_\psi \mathscr{E}(c,\psi)\ \phi \ \mathrm{d}\boldsymbol{x}. \tag{7}$$

From this we derive the coupled system for the time-dependent concentration $c : \mathbb{R}_{\geq 0} \times \Omega \to \mathbb{R}$ and the phase function $\psi : \mathbb{R}_{\geq 0} \times \Omega \to \mathbb{R}$

$$\partial_t c = \nabla \cdot \left(M(c)\ \nabla \delta_c \mathscr{E}(c,\psi)\right), \tag{8}$$

$$\partial_\tau \psi = \Delta\left(\delta_\psi \mathscr{E}(c,\psi)\right) \tag{9}$$

that evolve on two different time scales t and τ, respectively. It is assumed that ψ changes on a faster time scale requiring to take smaller time steps compared to c, that is, c remains constant when ψ evolves.

In order to derive the system of evolution for this energy, we need to develop the term $\delta_c \mathscr{E}(c,\psi)$, more precisely the expression resulting from the second integral in (7). For this we define, similar to the before, $\mathcal{J}_k(c) := \int_\Omega \psi(\beta\Delta)^k \psi \frac{1}{\beta}\ \mathrm{d}\boldsymbol{x}$ for $k = 0, \dots, 4$. In terms of the functions v, w, u, z introduced in Section 2, we find the simplified forms

$$\mathcal{J}_0(c) = \int_\Omega |\psi|^2 \frac{1}{\beta}\ \mathrm{d}\boldsymbol{x}, \qquad \mathcal{J}_1(c) = -\int_\Omega |\nabla\psi|^2\ \mathrm{d}\boldsymbol{x}, \qquad \mathcal{J}_2(c) = \int_\Omega \frac{1}{\beta}|v|^2\ \mathrm{d}\boldsymbol{x},$$

$$\mathcal{J}_3(c) = -\int_\Omega |\nabla v|^2\ \mathrm{d}\boldsymbol{x}, \qquad \mathcal{J}_4(c) = \int_\Omega \frac{1}{\beta}|w|^2\ \mathrm{d}\boldsymbol{x}.$$

We now calculate the functional derivative with respect to c and perturbation λ

$$\mathcal{J}_0'(c)[\lambda] = -\int_\Omega \frac{\beta'}{\beta^2}|\psi|^2\lambda, \qquad \mathcal{J}_1'(c)[\lambda] = 0, \qquad \mathcal{J}_2'(c)[\lambda] = \int_\Omega \frac{\beta'}{\beta^2}|v|^2\lambda,$$

$$\mathcal{J}_3'(c)[\lambda] = \int_\Omega 2\frac{\beta'}{\beta^2}vw\lambda, \qquad \mathcal{J}_4'(c)[\lambda] = \int_\Omega \frac{\beta'}{\beta^2}\left(|w|^2 + 2uv\right)\lambda,$$

where we again only consider the volume gradient for this part, that is, we neglect all boundary terms in the formal differentiation.

We finally obtain

$$\delta_c \mathscr{E}(c,\psi) = W'(c) - \kappa\Delta c + \frac{\gamma}{2}\left(-a_0|\psi|^2 + a_2|v|^2 + 2a_3vw + a_4\left(|w|^2 + 2uv\right) - \frac{1}{2}|w|^4\right)\frac{\beta'}{\beta^2}$$

and

$$\delta_\psi \mathscr{E}(c,\psi) = \frac{a_0}{\beta}\psi + \Delta\left(a_1\psi + a_2v + a_3w + a_4u\right) + \frac{1}{\beta}\psi^3.$$

The now resulting 10th-order parabolic equation (9) is reduced to a system of second order equations, which gives

$$\frac{1}{\beta(c)}v = \Delta\psi, \tag{10}$$

$$\frac{1}{\beta(c)}w = \Delta v, \tag{11}$$

$$\frac{1}{\beta(c)}u = \Delta w, \tag{12}$$

$$p = \frac{a_0}{\beta(c)}\psi + \Delta\left(a_1\psi + a_2 v + a_3 w + a_4 u\right) + \frac{1}{\beta(c)}\psi^3, \tag{13}$$

$$\partial_\tau \psi = \Delta p. \tag{14}$$

We define $\boldsymbol{z} = [\psi, v, w, u, p]$ and collect the equations (10)–(14) in a system of the form $\boldsymbol{\mathcal{R}} = \boldsymbol{0}$, with the components of $\boldsymbol{\mathcal{R}}$ being

$$\begin{aligned}
\boldsymbol{\mathcal{R}}_\psi(\boldsymbol{z})[\phi] &= (\partial_t\psi, \phi) + (\nabla p, \nabla\phi),\\
\boldsymbol{\mathcal{R}}_p(\boldsymbol{z})[\phi] &= (p, \phi) + (a_1\nabla\psi + a_2\nabla v + a_3\nabla w + a_4\nabla u, \nabla\phi) - \left(a_0\frac{\psi}{\beta(c)} + \frac{\psi^3}{\beta(c)}, \phi\right),\\
\boldsymbol{\mathcal{R}}_v(\boldsymbol{z})[\phi] &= (\nabla\psi, \nabla\phi) + \left(\frac{v}{\beta(c)}, \phi\right),\\
\boldsymbol{\mathcal{R}}_w(\boldsymbol{z})[\phi] &= (\nabla v, \nabla\phi) + \left(\frac{w}{\beta(c)}, \phi\right),\\
\boldsymbol{\mathcal{R}}_u(\boldsymbol{z})[\phi] &= (\nabla w, \nabla\phi) + \left(\frac{u}{\beta(c)}, \phi\right).
\end{aligned}$$

Here we used $(\cdot\,,\cdot)$ to denote the L^2-scalarproduct over Ω.

The combined scheme. As before, in Section 2, the above system of $\mathcal{R}$ is applicable for both periodic and zero flux boundary conditions and this defines the set of test functions ϕ. The following time-discretized system of equations with test functions $\phi_h \in V_h$ to perform the step from ψ^n to ψ^{n+1} via intermediate steps $\psi^{n+(j-1)/M}$ for $j = 1, \dots, M$ ($M \in \mathbb{N}$), is stated as follows

$$\boldsymbol{\mathcal{R}}_\psi(\boldsymbol{z})[\phi_h] = \left(\psi^{n+j/M} - \psi^{n+(j-1)/M}, \phi_h\right) + \tau\left(\nabla p^{n+j/M}, \nabla\phi_h\right), \tag{15}$$

$$\boldsymbol{\mathcal{R}}_p(\boldsymbol{z})[\phi_h] = \left(p^{n+j/M}, \phi_h\right) + \left(a_1\nabla\psi^{n+j/M} + a_2\nabla v^{n+j/M} + a_3\nabla w^{n+j/M} + a_4\nabla u^{n+j/M}, \nabla\phi_h\right) \tag{16}$$

$$- \frac{1}{\beta(c^{n+1})}\left(a_0\psi^{n+j/M} + 3\left(\psi^{n+(j-1)/M}\right)^2\psi^{n+j/M} - 2\left(\psi^{n+(j-1)/M}\right)^3, \phi_h\right), \tag{17}$$

$$\boldsymbol{\mathcal{R}}_v(\boldsymbol{z})[\phi_h] = \left(\nabla\psi^{n+j/M}, \nabla\phi_h\right) + \left(\frac{v^{n+j/M}}{\beta(c^{n+1})}, \phi_h\right),$$

$$\boldsymbol{\mathcal{R}}_w(\boldsymbol{z})[\phi_h] = \left(\nabla v^{n+j/M}, \nabla\phi_h\right) + \left(\frac{w^{n+j/M}}{\beta(c^{n+1})}, \phi_h\right), \tag{18}$$

$$\boldsymbol{\mathcal{R}}_u(\boldsymbol{z})[\phi_h] = \left(\nabla w^{n+j/M}, \nabla\phi_h\right) + \left(\frac{u^{n+j/M}}{\beta(c^{n+1})}, \phi_h\right). \tag{19}$$

Note that the state of c is constant during these intermediate steps as already remarked.

As in Section 3, the fourth-order parabolic equation (8) is reduced into a system of second-order equations. For this we let

$$\begin{aligned}
\partial_t c &= \nabla\cdot\left(M(c)\nabla\left(\mu + \gamma\eta\right)\right),\\
\mu &= W'(c) - \kappa\Delta c,\\
\eta &= \frac{1}{2}\left(-a_0|\psi|^2 + a_2|v|^2 + 2a_3 vw + a_4\left(|w|^2 + 2uv\right) - \frac{1}{2}|w|^4\right)\frac{\beta'(c)}{\beta(c)^2}.
\end{aligned}$$

We define $\boldsymbol{z} = [c, \mu, \eta]$ and collect the equations in a system of the form $\boldsymbol{\mathcal{R}} = \boldsymbol{0}$, with the components of $\boldsymbol{\mathcal{R}}$ being

$$\begin{aligned}
\boldsymbol{\mathcal{R}}_\mu(\boldsymbol{z})[\phi] &= (\partial_t c, \phi) + (\nabla\mu, \nabla\phi) + \gamma(\nabla\eta, \nabla\phi) - \langle \nu\cdot M(c)\nabla\mu, \phi\rangle,\\
\boldsymbol{\mathcal{R}}_c(\boldsymbol{z})[\phi] &= \left(W'(c), \phi\right) - (\mu, \phi) + \kappa(\nabla c, \nabla\phi),\\
\boldsymbol{\mathcal{R}}_\eta(\boldsymbol{z})[\phi] &= (\eta, \phi) - \left(\frac{1}{2}\left(-a_0|\psi|^2 + a_2|v|^2 + 2a_3 vw + a_4\left(|w|^2 + 2uv\right) - \frac{1}{2}|w|^4\right)\frac{\beta'(c)}{\beta(c)^2}, \phi\right),
\end{aligned}$$

where $\langle\cdot,\cdot\rangle$ denoted the L^2-scalar product on $\partial\Omega$, the constant normal flux is taken as $J = \nu\cdot M(c)\nabla\mu$, and η has a zero flux boundary condition.

The above system is solved implicitly and the time discretized system of equations with test functions $\phi_h \in V_h$ is stated as follows

$$\mathcal{R}_\mu(\boldsymbol{z})[\phi_h] = \left(c^{n+1} - c^n, \phi_h\right) + \triangle t \left(M(c^{n+1})\nabla\mu^{n+1}, \nabla\phi_h\right) + \triangle t\, \gamma \left(M(c^{n+1})\nabla\eta^{n+1}, \nabla\phi_h\right) - \triangle t \left\langle J, \phi_h\right\rangle, \tag{20}$$

$$\mathcal{R}_c(\boldsymbol{z})[\phi_h] = \left(W'(c^{n+1}), \phi_h\right) - \left(\mu^{n+1}, \phi_h\right) + \kappa \left(\nabla c^{n+1}, \nabla\phi_h\right), \tag{21}$$

$$\mathcal{R}_\eta(\boldsymbol{z})[\phi_h] = \left(\eta^{n+1}, \phi_h\right) - \left(\frac{1}{2}\left(-a_0|\psi^n|^2 + a_2|v^n|^2 + 2a_3v^nw^n + a_4\left(|w^n|^2 + 2u^nv^n\right) - \frac{1}{2}|w^n|^4\right)\frac{\beta'(c^{n+1})}{\beta(c^{n+1})^2}, \phi_h\right). \tag{22}$$

We note that the time step τ used to evolve 2MPFC introduces a pseudo-time primarily to relax the system. In Reference 25, it was proposed that for each CH time step $\triangle t$, the PFC model is evolved till the system equilibrium $\delta_\psi \mathscr{E} \approx 0$ is approximately reached. However, such a criterion would result in an overall equilibrium of the PFC system without further need for minimization. Instead, it is the stress induced due to lattice expansion for each CH time step that needs to be at equilibrium.[41] However, computing stress would require expressing ψ in terms of amplitudes (1) and solving for the amplitudes as it is done in References 27,42, and 43 for 1MPFC models. But the amplitude formulation for 2MPFC has not yet been accomplished and such a formulation would be beyond the scope of the current work. Here, we have equally divided each time step $\triangle t$ into intervals of length τ, assuming that $\triangle t$ is large enough for the dynamics of τ to reach equilibrium.

5 | NUMERICAL RESULTS FOR PHASE-SEPARATION

In this section, we apply the developed formulations to study phase-separation in an electrode particle. During lithiation of the electrode the particle swells, which can cause structural transformation in the electrode material. The expansion coefficient is defined as $\alpha(\chi) = \alpha_{\mathrm{MO}} + (\alpha_{\mathrm{LMO}} - \alpha_{\mathrm{MO}})\chi$ for $\chi \in (0,1)$. The MO and LMO parameters for lattice expansion taken from Reference 7 are listed in Table 3, whereas the pictorial representation of the expansion can be seen in Figure 1(A).

2MFPC formulation. First the proposed 2MFPC formulation (15)–(19) is tested before we study the effect of chemical cycle. We consider the domain $\Omega = [-200, 200]^2$ and apply homogeneous Neumann conditions on all variables, that is, ψ, v, w, u, and p at $\partial\Omega$. The parameters in the free energy functional are taken as $\beta = 1.0$ (no expansion), $\varepsilon = 0.15$, and $Q = \sqrt{2}$. The system is initialized for ψ_h^0 with random numbers between −0.5 and 0.1, as seen in Figure 2(A), and with the other variables set to zero. We employed linear Lagrange elements and a constant time step size of one to evolve in time. A grid size of 0.8 is used to discretize the spatial domain. The 2MPFC system (15)–(19) was solved using the Jacobian-free Newton–Krylov method (JFNK)[45] preconditioned with block diagonals.[46]

As seen from the 2MPFC phase diagram in Figure 1(B), there are two stable solid phases, namely, hexagonal and square. This is exhibited in Figure 2(B) at time 150 where a mixture of both phases can be noticed. As time evolves the square phase grows at the expense of the hexagonal phase as seen in Figure 2(C) at time 600. This phenomenon was previously observed by Shuai et al.[38] during their study on hexagonal-to-square phase transitions. Finally at time 1200, we see a polycrystalline structure composed only of square lattices with different orientations. This demonstrates the applicability of the proposed mixed formulation for the 2MPFC model.

2MFPC and Cahn–Hilliard. The 2MPFC system (15)–(19) is now coupled with CH (20)–(22) to study phase-separation in LMO. The material properties for LMO listed in Table 4 are taken from Huttin et al.[3]

We consider a particle given by $\Omega = [-L_0, L_0]^2$ and apply a constant normal flux J on the particle surface in order to completely lithiate the particle in 1 hour. This flux J is calculated to

$$J = \frac{C_{rate}C_{max}L_0}{2 \cdot 3600} = 0.0277.$$

This serves as a non-homogeneous Neumann condition on the boundary of the particle. The sign of the flux determines whether the particle is lithiated or delithiated. Here, we assign a positive sign for lithiation. An initial state of $c(0) = 0.001$ is

TABLE 3 Lattice constants

Electrode	a (nm)	b (nm)	α
Mn_2O_4 (MO)	80.3	80.3	1.0
$Li_xMn_2O_4$ (LMO)	82.692	82.692	1.0297

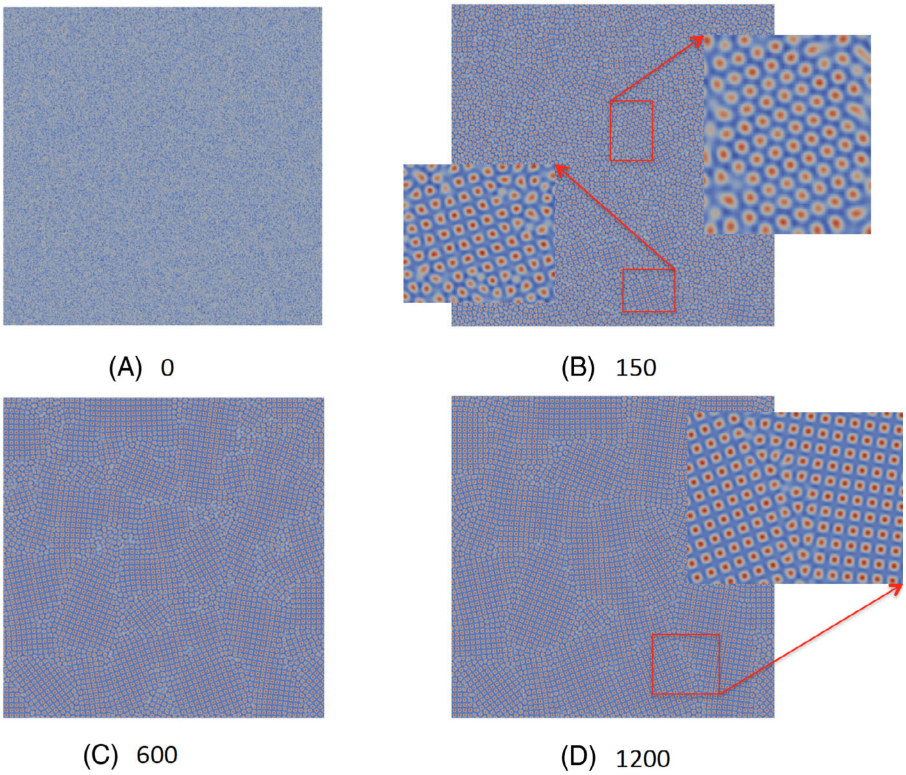

FIGURE 2 Time evolution of two-mode phase field crystal model (with homogeneous Neumann boundary conditions) at selected times 0, 150, 600, 1200

TABLE 4 Material parameters[3]

Parameter	Value	Unit	Non-dim form
l_0	$25 \cdot 10^{-10}$	m	1
t_0	1	sec	1
L_0	$0.5 \cdot 10^{-6}$	m	200
D_0	$7.08 \cdot 10^{-15}$	m^2/s	1132.8
κ	$7 \cdot 10^{-16}$	$1/m^2$	112
C_{max}	$2.29 \cdot 10^4$	mol/m^3	1
α_1	2.5	–	
α_2	-5.2	–	
C_{rate}	1	–	

assigned to avoid numerical blow-up due to the presence of the logarithmic term in the multiwell potential W. Physically such an assumption is not unreasonable as particles are hardly in a perfect zero lithiated state, whereas for μ an initial value of zero is assigned. The value of γ is taken as $1 \cdot 10^{-4}$. The spatial discretization adopted is the same as before, whereas the adaptive time stepping method of Reference 47 is used to evolve in time. The poly-crystalline state, as shown in Figure 2(D), is selected as the initial state for ψ_h^0 before lithiation. It can be seen that the polycrystal consists of grains of many different orientations with each grain having a square lattice structure.

The coupled 2PFC–CH system is evolved and in Figure 3 we present different status of charge (SOC) by concentration plots. It takes 1 hour for the particle to completely lithiate. Next we observe the changes in the crystal structure due to lithiation of the electrode particle. This is done by comparing the crystal structure of a lithiated particle from the 2MPFC–CH system to a crystal structure, which is not lithiated from the 2MPFC system evolved for the same duration. The comparison of the two crystal structures is shown in Figure 4. The change in crystal structure is primarily governed by grain boundary (GB) migration, which is induced by the reduction of GB curvature.[48] This is observed by the GB marked as red and in all GB motions from the 2MPFC simulation runs, which further validates the formulation. It can be seen in Figure 4(A) that interior grains demarcated green shrunk faster and disappeared in Figure 4(B), leading to the conclusion

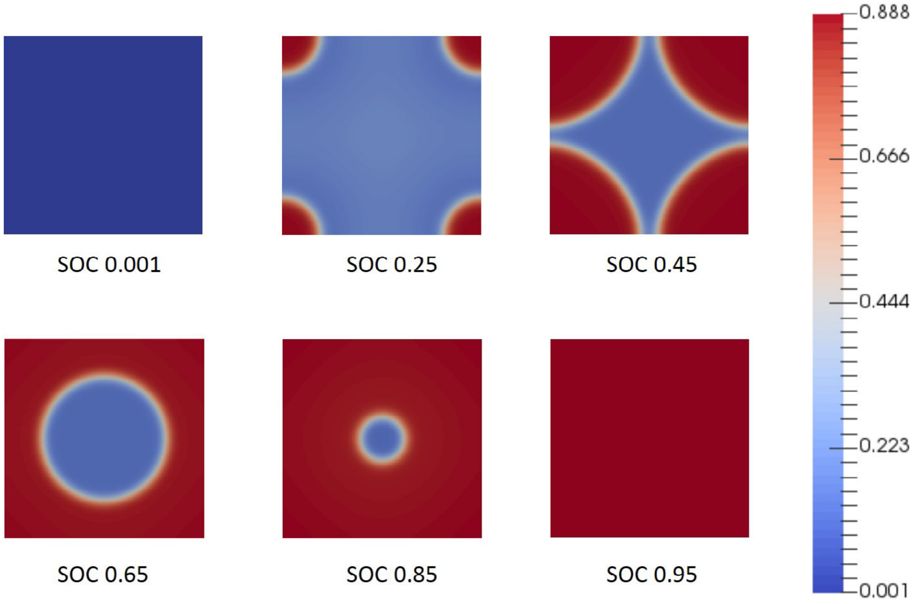

FIGURE 3 Lithiation of electrode particle using the 2MPFC–CH model at different status of charge (SOC) due to the application of a constant flux boundary condition

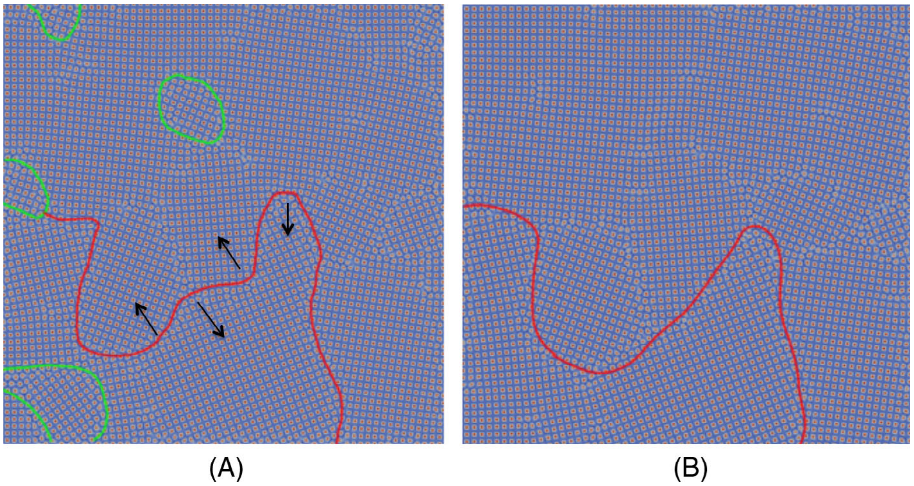

FIGURE 4 Comparison of crystal structure at 1 hour from (A) 2MPFC and (B) 2MPFC–CH

that there is grain boundary acceleration due to lithiation. This phenomenon was also reported in Reference 25 during the lithiation of $FePO_4/Li_xFePO_4$ electrode particles.

In order to access the volume change achieved during lithiation of the electrode particle, in Figure 5, the averaged α is plotted as a function of SOC. It was found that for SOC at 0.97 the volume change is 2.88%.

Now the electrode structure in Figure 4(B) is taken as the initial state before delithiation. A constant normal flux of $J = -0.0277$ is applied as Neumann condition on the boundary to delithiate the particle for an hour at $C_{\text{rate}} = 1$. The initial concentration field is taken as the one from Figure 3 at SOC 0.95. The coupled 2MPFC–CH system is evolved. The evolution of the concentration seen in Figure 6 exhibits similar behavior as observed during lithiation. A final comparison between the crystal structure from the 2MPFC–CH and 2MPFC systems after the same duration can be seen in Figure 7. As before the interior grains demarcated as green in Figure 7(A) have fully disappeared from the crystal structure in Figure 7(B), leading to the same conclusion that there is grain boundary acceleration. It is noted that the chemical cycle accelerates the GB migration and the process is not reversed.

It is noted that no real PFC material parameters were used to model LMO, due to the lack of availability of such data. Using the correct parameters to model materials is one of the challenges facing the PFC community in general. There are a few exceptions. In Reference 37, for instance, elastic constants using two-mode PFC model for fcc Ni and one-mode PFC model for bcc Fe were predicted, but showed disagreements with MD simulations. In a recent attempt there was more success by using a fractional-Laplacian[49] in the free energy functional and by fitting it to the first order peak in experimental measurements of the structure factor to model Cu, Al, In, Ti, Sn, and Pb. However, such a formulation is

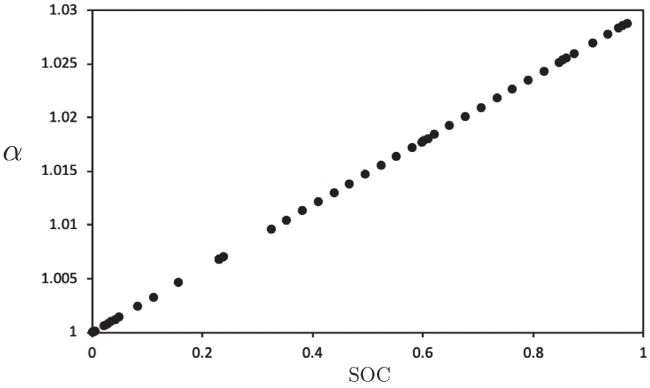

FIGURE 5 The averaged α over the domain achieved during lithiation of the electrode particle as a function of status of charge (SOC)

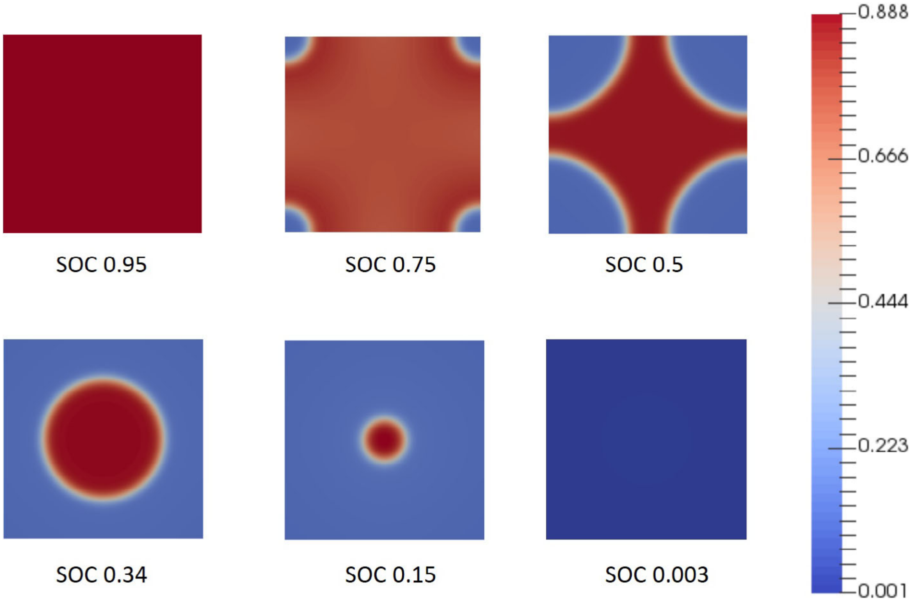

FIGURE 6 Delithiation of electrode particle using 2MPFC–CH model at different states of charge (SOC) due to the application of a constant flux boundary condition

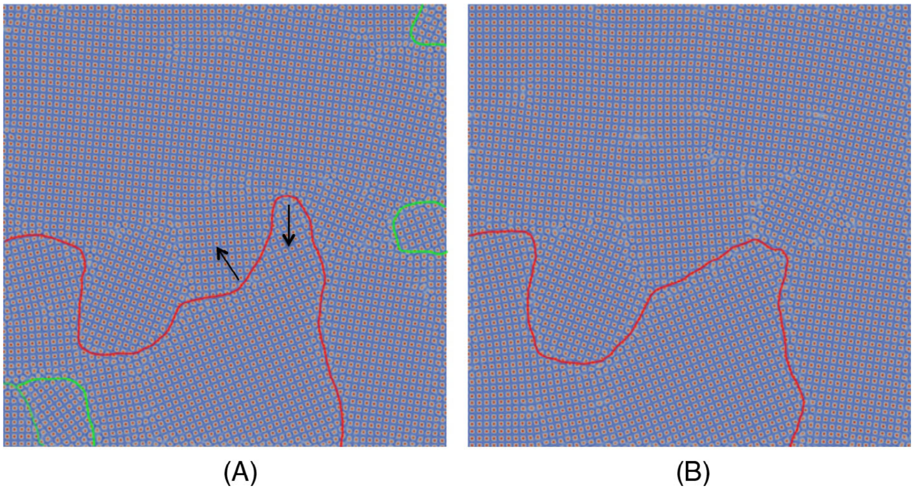

FIGURE 7 Comparison of crystal structure at 2 hours from (A) 2MPFC and (B) 2MPFC–CH

not widely adopted. In the current work, major focus has been on capturing the correct crystal symmetries of LMO and lattice expansion due to lithiation. We report here, although only qualitative, that there is grain growth due to lithiation in LMO. This phenomenon was also observed by Reference 25 in the lithiation of LFPO. In a recent study,[50] it was found that external magnetic fields can support grain coarsening in polycrystalline structures. It can be said that perturbing grain boundaries due to external fields can in general lead to the acceleration of grain growth.

6 | CONCLUSIONS

The proposed mixed finite element formulation for 2MPFC system is demonstrated to produce a square lattice structure in 2D to model LMO. The 2MPFC–CH allows to study phase separation in electrode particles by taking into account the crystallographic changes in the host material during chemical cycle. The multiscale system is solved using a semi-implicit scheme. Numerical results show that there is an acceleration of grain boundary migration due to lithiation of the electrode particle. The coupling terms also include anisotropic phase separation effects via the term $\gamma \frac{\psi}{2} G(\beta\Delta)\psi$ in the free energy functional. For larger values of γ, the evolution of ψ can also in-return influence the diffusion of concentration. As 2MPFC free energy functional includes the contribution of elastic energy, it is yet to be verified if mechanical equilibrium is established at every time. In the future, we would incorporate the work of Skaugen et al.[41] into 2MPFC to account for the separation of elastic and plastic time scales.

ACKNOWLEDGMENTS

K. Chockalingam gratefully acknowledges financial support by the German Research Foundation (DFG) through RTG 2218 Simulation of Mechano-Electro-Thermal processes in Lithium-Ion-Batteries (SiMET), project number 281041241. Open Access funding enabled and organized by Projekt DEAL.

DATA AVAILABILITY STATEMENT

All data are available from the corresponding author by request.

ORCID

Willy Dörfler https://orcid.org/0000-0003-1558-9236

REFERENCES

1. Bruce PG. Energy storage beyond the horizon: rechargeable lithium batteries, *Solid State Ionics* 2008; 179(21): 752-760. Solid State Ionics 16: Proceedings of the 16th International Conference on Solid State Ionics (SSI-16) Part I. https://doi.org/10.1016/j.ssi.2008.01.095
2. Tarascon JM, Armand M. Issues and challenges facing rechargeable lithium batteries. *Nature*. 2001;414(6861):359-367. https://doi.org/10.1038/35104644.
3. Huttin M, Kamlah M. Phase-field modeling of stress generation in electrode particles of lithium ion batteries. *Appl Phys Lett*. 2012;101(13):133902. https://doi.org/10.1063/1.4754705.
4. Zhang T, Kamlah M. A nonlocal species concentration theory for diffusion and phase changes in electrode particles of lithium ion batteries. *Contin Mech Thermodyn*. 2018;30(3):553-572. https://doi.org/10.1007/s00161-018-0624-z.
5. Meethong N, Kao YH, Tang M, Huang HY, Carter WC, Chiang YM. Electrochemically induced phase transformation in nanoscale olivines Li1-xMPO4 (M = Fe, Mn). *Chem Mater*. 2008;20(19):6189-6198. https://doi.org/10.1021/cm801722f.
6. Li Q, Yao Z, Lee E, et al. Dynamic imaging of crystalline defects in lithium-manganese oxide electrodes during electrochemical activation to high voltage. *Nat Commun*. 2019;10(1):1692. https://doi.org/10.1038/s41467-019-09408-2.
7. Sato K, Poojary D, Clearfield A, Kohno M, Inoue Y. The surface structure of the proton-exchanged lithium manganese oxide spinels and their lithium-ion sieve properties. *J Solid State Chem*. 1997;131(1):84-93. https://doi.org/10.1006/jssc.1997.7348.
8. Hillert M, Purdy GR. Chemically induced grain boundary migration. *Acta Metall*. 1978;26(2):333-340. https://doi.org/10.1016/0001-6160(78)90132-3.
9. Christensen J, Newman J. A mathematical model of stress generation and fracture in lithium manganese oxide. *J Electrochem Soc*. 2006;153(6):A1019-A1030. https://doi.org/10.1149/1.2185287.
10. Lee E, Lee KR, Lee BJ. Interatomic potential of Li-Mn-O and molecular dynamics simulations on Li diffusion in spinel Li1-xMn2O4. *J Phys Chem C*. 2017;121(24):13008-13017. https://doi.org/10.1021/acs.jpcc.7b02727.
11. Xiao R, Li H, Chen L. Density functional investigation on Li2MnO3. *Chem Mater*. 2012;24(21):4242-4251. https://doi.org/10.1021/cm3027219.
12. Zhai H. Modeling of lithium-ion battery for charging/discharging characteristics based on circuit model. *Int J Online Biomed Eng*. 2017;13(6):86-95. https://doi.org/10.3991/ijoe.v13i06.6799.
13. Lu CH, Lin SW. Influence of the particle size on the electrochemical properties of lithium manganese oxide. *J Power Sources*. 2001;97-98:458-460. Proceedings of the 10th International Meeting on Lithium. https://doi.org/10.1016/S0378-7753(01)00637-1.

14. Chen LQ. Phase-field models for microstructure evolution. *Annu Rev Mater Res*. 2002;32(1):113-140. https://doi.org/10.1146/annurev.matsci.32.112001.132041.
15. Moelans N, Blanpain B, Wollants P. An introduction to phase-field modeling of microstructure evolution. *Calphad*. 2008;32(2):268-294. https://doi.org/10.1016/j.calphad.2007.11.003.
16. Tadmor EB, Ortiz M, Phillips R. Quasicontinuum analysis of defects in solids. *Philos Mag A*. 1996;73(6):1529-1563. https://doi.org/10.1080/01418619608243000.
17. Kohlhoff S, Gumbsch P, Fischmeister HF. Crack propagation in b.c.c. crystals studied with a combined finite-element and atomistic model. *Philos Mag A*. 1991;64(4):851-878. https://doi.org/10.1080/01418619108213953.
18. Novick-Cohen A, Segel LA. Nonlinear aspects of the Cahn-Hilliard equation. *Phys D Nonlinear Phenomena*. 1984;10(3):277-298. https://doi.org/10.1016/0167-2789(84)90180-5.
19. Elder K, Grant M. Modeling elastic and plastic deformations in nonequilibrium processing using phase field crystals. *Phys Rev E Stat Nonlinear Soft Matter Phys*. 2004;70:051605. https://doi.org/10.1103/PhysRevE.70.051605.
20. Swift J, Hohenberg PC. Hydrodynamic fluctuations at the convective instability. *Phys Rev A*. 1977;15:319-328. https://doi.org/10.1103/PhysRevA.15.319.
21. Skaugen A. *A Unified Perspective on Two-dimensional Quantum Turbulence and Plasticity* [PhD thesis]. Faculty of Mathematics and Natural Sciences, University of Oslo; 2018.
22. Adland AJ. *Phase-Field Crystal Modeling of Polycrystalline Materials* [PhD thesis]. Boston, MA: Northeastern University; 2013.
23. Emmerich H, Löwen H, Wittkowski R, et al. Phase-field-crystal models for condensed matter dynamics on atomic length and diffusive time scales: an overview. *Adv Phys*. 2012;61(6):665-743. https://doi.org/10.1080/00018732.2012.737555.
24. Skaugen A, Angheluta L. Dislocation dynamics and crystal plasticity in the phase-field crystal model. *Phys Rev B*. 2018;97:054113. https://doi.org/10.1103/PhysRevB.97.054113.
25. Balakrishna AR, Chiang YM, Carter WC. Phase-field model for diffusion-induced grain boundary migration: an application to battery electrodes. *Phys Rev Mater*. 2019;3:065404. https://doi.org/10.1103/PhysRevMaterials.3.065404.
26. Mellenthin J, Karma A, Plapp M. Phase-field crystal study of grain-boundary premelting. *Phys Rev B*. 2008;78:184110. https://doi.org/10.1103/PhysRevB.78.184110.
27. Salvalaglio M, Backofen R, Voigt A, Elder K. Controlling the energy of defects and interfaces in the amplitude expansion of the phase-field crystal model. *Phys Rev E*. 2017;96:023301. https://doi.org/10.1103/PhysRevE.96.023301.
28. Athreya BP, Goldenfeld N, Dantzig JA. Renormalization-group theory for the phase-field crystal equation. *Phys Rev E*. 2006;74:011601. https://doi.org/10.1103/PhysRevE.74.011601.
29. Balakrishna AR, Carter WC. Combining phase-field crystal methods with a Cahn-Hilliard model for binary alloys. *Phys Rev E*. 2018;97:043304. https://doi.org/10.1103/PhysRevE.97.043304.
30. Backofen R, Rätz A, Voigt A. Nucleation and growth by a phase field crystal (PFC) model. *Philos Mag Lett*. 2007;87(11):813-820. https://doi.org/10.1080/09500830701481737.
31. Brenner S, Scott R. *The Mathematical Theory of Finite Element Methods*. New York, NY: Springer; 2007.
32. Belytschko T, Liu WK, Moran B, Elkhodary K. *Nonlinear Finite Elements for Continua and Structures*. Hoboken, NJ: Wiley; 2014.
33. Bai Y, Zhao Y, Liu W, Xu BX. Two-level modeling of lithium-ion batteries. *J Power Sources*. 2019;422:92-103. https://doi.org/10.1016/j.jpowsour.2019.03.026.
34. Praetorius S, Voigt A. Development and analysis of a block-preconditioner for the phase-field crystal equation. *SIAM J Sci Comput*. 2015;37(3):B425-B451. https://doi.org/10.1137/140980375.
35. Gomez H, Nogueira X. An unconditionally energy-stable method for the phase field crystal equation. *Comput Methods Appl Mech Eng*. 2012;249-252:52-61. https://doi.org/10.1016/j.cma.2012.03.002.
36. Zhang J, Yang X. On efficient numerical schemes for a two-mode phase field crystal model with face-centered-cubic (FCC) ordering structure. *Appl Numer Math*. 2019;146:13-37. https://doi.org/10.1016/j.apnum.2019.06.017.
37. Wu KA, Adland A, Karma A. Phase-field-crystal model for fcc ordering. *Phys Rev E*. 2010;81:061601. https://doi.org/10.1103/PhysRevE.81.061601.
38. Shuai X, Mao H, Kong Y, Du Y. Phase field crystal simulation of the structure evolution between the hexagonal and square phases at elevated pressures. *J Min Metall Sect B Metall*. 2017;53:271-278.
39. Gaston D, Newman C, Hansen G, Lebrun-Grandié D. MOOSE: a parallel computational framework for coupled systems of nonlinear equations. *Nucl Eng Des*. 2009;239(10):1768-1778. https://doi.org/10.1016/j.nucengdes.2009.05.021.
40. Copetti MIM, Elliott CM. Numerical analysis of the Cahn-Hilliard equation with a logarithmic free energy. *Numer Math*. 1992;63(1):39-65.
41. Skaugen A, Angheluta L, Viñals J. Separation of elastic and plastic timescales in a phase field crystal model. *Phys Rev Lett*. 2018;121:255501. https://doi.org/10.1103/PhysRevLett.121.255501.
42. Ainsworth M, Mao Z. Phase field crystal based prediction of temperature and density dependence of elastic constants through a structural phase transition. *Phys Rev B*. 2019;100:104101. https://doi.org/10.1103/PhysRevB.100.104101.
43. Salvalaglio M, Angheluta L, Huang ZF, Voigt A, Elder KR, Viñals J. A coarse-grained phase-field crystal model of plastic motion. *J Mech Phys Solids*. 2020;137:103856. https://doi.org/10.1016/j.jmps.2019.103856.
44. Emdadi A, Zaeem MA, Asadi E. Revisiting phase diagrams of two-mode phase-field crystal models. *Comput Mater Sci*. 2016;123:139-147. https://doi.org/10.1016/j.commatsci.2016.06.018.
45. Knoll D, Keyes D. Jacobian-free Newton–Krylov methods: a survey of approaches and applications. *J Comput Phys*. 2004;193(2):357-397. https://doi.org/10.1016/j.jcp.2003.08.010.

46. Chockalingam K, Tonks MR, Hales JD, Gaston DR, Millett PC, Zhang L. Crystal plasticity with Jacobian-Free Newton–Krylov. *Comput Mech*. 2013;51(5):617-627. https://doi.org/10.1007/s00466-012-0741-7.
47. Tonks MR, Gaston D, Millett PC, Andrs D, Talbot P. An object-oriented finite element framework for multiphysics phase field simulations. *Comput Mater Sci*. 2012;51(1):20-29. https://doi.org/10.1016/j.commatsci.2011.07.028.
48. Winning M, Gottstein G, Shvindlerman L. On the mechanisms of grain boundary migration. *Acta Mater*. 2002;50(2):353-363. https://doi.org/10.1016/S1359-6454(01)00343-3.
49. Ainsworth M, Mao Z. Fractional phase-field crystal modelling: analysis, approximation and pattern formation. *IMA J Appl Math*. 2020;85(2):231-262. https://doi.org/10.1093/imamat/hxaa004.
50. Backofen R, Voigt A. Magnetically induced/enhanced coarsening in thin films. *Phys Rev Mater*. 2020;4:023404. https://doi.org/10.1103/PhysRevMaterials.4.023404.

How to cite this article: Chockalingam K, Dörfler W. Implementation of the coupled two-mode phase field crystal model with Cahn–Hilliard for phase-separation in battery electrode particles. *Int J Numer Methods Eng*. 2021;1–15. https://doi.org/10.1002/nme.6632